Dalton Transactions

ROYAL SOCIETY OF CHEMISTRY

PAPER

View Article Online
View Journal | View Issue

Cite this: *Dalton Trans.*, 2024, **53**, 14648

Enhanced photovoltaic performance of silicon solar cells using a down-shift $KCa_2Mg_2(VO_4)_3$ phosphor†

Hong Su,[a] Cong Dou,[a] Fan Dou,[b] Wen Li,[a] Jiachen Li,[a] Xiaolian Chao,[c] Zupei Yang,[c] Xiaoming Wang *[a] and Huan Jiao *[a]

Received 22nd June 2024,
Accepted 22nd July 2024

DOI: 10.1039/d4dt01814a

rsc.li/dalton

The efficiency of silicon solar cells is still lower than theoretical values, partly due to their inability to utilize the ultraviolet and infrared portions of the solar spectrum. Herein, a novel method using a $KCa_2Mg_2(VO_4)_3$ phosphor with a down-shift effect to improve the photovoltaic performance of silicon solar cells and enhance the utilization of UV light in standard p-type silicon solar cells is proposed. The synthesized phosphors were mixed with an ethylene vinyl acetate (EVA) copolymer and pressed into a film, which was subsequently encapsulated in monocrystalline silicon solar cells. The results show that the addition of this film notably enhanced the photovoltaic performance of the silicon solar cells; the current density was increased by 2.89% (from 33.20 to 34.16 mA cm^{-2}), and the photovoltaic conversion efficiency was improved by 5.69% (from 15.11% to 15.97%) at the optimal concentration compared to bare cells.

1. Introduction

Recently, the rise of artificial intelligence has ushered in a new direction for the industrial revolution, along with new demands for energy consumption. Among the new renewable energy sources, solar energy is undoubtedly one of the most suitable types to meet the current needs of artificial intelligence.[1] Compared to other renewable energy sources, solar energy has the advantages of being abundant, environmentally friendly, pollution-free, and widely applicable, and having a low maintenance cost.[2–5] However, the proportion of solar energy in the total energy consumption is still very low, necessitating the development of more efficient and cheaper photovoltaic devices. In the research aimed at improving the photoelectric conversion efficiency of solar energy, crystalline silicon solar cells primarily absorb solar radiation in the wavelength range of 400–1100 nm.[6–8] In the ultraviolet (UV) and infrared (IR) regions, the absorption of silicon solar cells is very weak, resulting in insufficient utilization of these photons. Therefore, it is imperative to further optimize the absorption spectrum of silicon solar cells in photovoltaic applications to enhance the photoelectric conversion efficiency of solar energy and achieve large-scale energy utilization.[9–12] Placing a conversion layer on the bottom of the solar cell absorbs and converts low-energy photons, re-emitting them to the solar cell at a usable wavelength. The secondary absorption and utilization of low-energy infrared photons can effectively reduce the temperature of the battery. However, current up-conversion (UC) fluorescent materials with Er^{3+}, Yb^{3+}–Er^{3+}, and Yb^{3+}–Ho^{3+} as the luminescence center mostly have linear excitation and emission spectra, resulting in a larger part of the spectrum being wasted in the form of thermal radiation.[13–16] Another method to modify the solar spectrum is to use down-conversion (DC) or down-shift (DS) methods to generate low-energy photons from high-energy photons to improve the absorption of silicon solar cells in the UV region. The absorption of high-energy photons by the DC/DS layer will extend the life of the solar cell, while the release of low-energy photons will enhance the photoelectric conversion efficiency within the available wavelength band.[17,18] Selecting spectral conversion materials that match the optimal wavelength for crystalline silicon absorption in diverse DC/DS systems is crucial for achieving a net increase in efficiency.[19–27] The application of phosphors in solar cells is also critical, as different methods can yield significantly varying results. Elleuch *et al.* achieved down-conversion by placing Er^{3+}-doped ZnO thin films on the surface of silicon solar cells.[28] However, the deposition process required for these thin films is complex and can affect the structure of the solar cells. Aouaini *et al.* accomplished spectral conversion by

[a]*Key Laboratory of Macromolecular Science of Shaanxi Province, Shaanxi Key Laboratory for Advanced Energy Devices, Shaanxi Engineering Laboratory for Advanced Energy Technology, School of Chemistry & Chemical Engineering, Shaanxi Normal University, Xi'an, Shaanxi, 710062, P. R. China. E-mail: jiaohuan@snnu.edu.cn, xmwang@snnu.edu.cn*

[b]*Yantai Shied Materials Technology Co., Ltd, Development Zone, Yantai 264006, Shandong Province, P. R. China*

[c]*School of Materials Science and Engineering, Shaanxi Normal University, Xi'an, Shaanxi, 710062, P. R. China*

†Electronic supplementary information (ESI) available. See DOI: https://doi.org/10.1039/d4dt01814a

doping Er^{3+} ions into tellurite glass, which is also a complicated process that increases production costs.[29] Karunakaran *et al.* mixed Ce^{3+}-doped YAG with Ce^{3+}–Yb^{3+}-co-doped YAG, then combined it with an ethylene vinyl acetate copolymer (EVA) and applied it to the surface of silicon solar cells, resulting in a maximum increase in the solar cell efficiency of 4.19%.[30] Liu *et al.* enhanced the performance of silicon solar cells by combining Eu^{3+} with organic ligands and adding it to PVA as a coating, and the efficiency of the photovoltaic modules increased from 16.05% to 16.37%.[31] However, neither spin coating nor the use of organic ligands is an ideal application method. The cost of the spin coating process is high and the instability of organic ligands raises concerns about the device's lifespan.[32] According to the structure of the solar cell, we choose to combine the phosphor with EVA, which has excellent optical properties, good thermal stability and strong adhesion, to form a composite layer and place it in the solar cell, and the composite layer absorbs the short-wave part of the solar spectrum and converts it into the long-wave part, thereby improving the conversion efficiency and service life of the solar cell.

In this work, we designed a spectrum conversion film that not only acts as an adhesive for cell components, but also addresses the solar spectrum mismatch problem in solar cells. We selected the $KCa_2Mg_2(VO_4)_3$ (KCMV) phosphor for its UV self-excited broadband luminescence and quantum efficiency of 38.4%.[33–37] The phosphor combined with EVA showed a spectral transmittance equivalent to that of a single EVA film (90%). Solar cells combined with p-type monocrystalline silicon cells exhibited a notable improvement in their photoelectric conversion efficiency.

2. Experimental

2.1 Materials and synthesis

The polycrystalline powder sample KCMV was synthesized using the high-temperature solid-state method. The raw materials of $CaCO_3$ (Aladdin, 99%), K_2CO_3 (Aladdin, 99%), MgO (Aladdin, 99.9%) and V_2O_5 (Aladdin, 99%) were weighed according to the correct stoichiometry and mixed thoroughly in a polytetrafluoroethylene jar (100 mL) containing ethanol solvent for 24 hours using a plenary high-energy ball-milling machine with zirconia balls (∅ = 6, 8, and 10 mm). The ball milling process included 30 minutes of milling and 10 minutes of resting for each cycle with a ball milling speed controlled at 250 rpm. The fully mixed raw materials were dried and transferred to a muffle furnace in a corundum crucible, which was fired at 900 °C for 12 hours with a heating and cooling speed of 10 °C min^{-1}. The sintered samples were then ground into powder for subsequent testing.

2.2 Preparation of EVA/KCMV composite films and their encapsulation with solar cells

Due to the non-uniform particle size of the powder sample, the sample needed to be dispersed in ethyl alcohol solvent and then sieved through screens of different sizes (2000 and 2300 meshes) to obtain a uniform composite film after mixing with EVA. The mixture of the screened KCMV phosphors and EVA, according to different mass ratios, was heated at 140 °C. The well-mixed materials were pressed in a vacuum environment at 160 °C to form a film with a thickness of 0.4 mm. The film was cut into appropriate sizes and placed into a laminator (HongZheng machinery HZ-CYB, China) for encapsulation processing together with photovoltaic glass and commercial p-type monocrystalline silicon cells (Sunshine Science and Education Energy, China, 39.5 × 39.25 mm) at 150 °C (Fig. 1).

2.3 Characterization

The X-ray diffraction (XRD) measurement of KCMV was performed using a Rigaku Corporation MiniFlex600 X-ray diffractometer with Cu Kα radiation operated at 40 kV and 15 mA. TOPAS 5.0 software was used to refine the XRD data, which were collected over a 2θ range of 5–120° with a step size of 0.01° and a scanning speed of 0.0167° s^{-1}.[38] The photoluminescence (PL) and photoluminescence excitation (PLE) spectra of the KCMV phosphor were recorded using a Hitachi F7100 fluorescence spectrophotometer over a spectral range of 200–800 nm.[39] The variable-temperature PL spectra were recorded using an Edinburgh FLS920 spectrophotometer over the 370–800 nm spectral range at an interval of 25 °C from room temperature to 150 °C. The photoluminescence quantum yield (PLQY) of the KCMV phosphor was measured using a Hamamatsu C9920-02 PL quantum yield measurement system. The micromorphology of the phosphor powder after screening was analyzed using a field emission scanning electron microscope (FE-SEM, HITACHI SU8220). The X-ray photoelectron spectroscopy (XPS) data were obtained using an Axis UltraDLD XPS spectrometer (Britain). The electron paramagnetic resonance (EPR) measurement of the powder sample was performed at room temperature using a Bruker E500 spectrometer with a dual-mode microwave cavity. The four-electrode method was used to record the volt–ampere characteristic curves of solar cells with and without a DS spectrum conversion layer under standard solar irradiation (100 mW cm^{-2}) at 25 °C using an AAA-level xenon solar simulator (Zolix ss150, China) in conjunction with a digital source meter (Keithley 2400, USA). The reflectance, absorption and transmission spectra of spectral conversion films and solar cell modules were recorded using a PerkinElmer Lambda1050 UV-visible

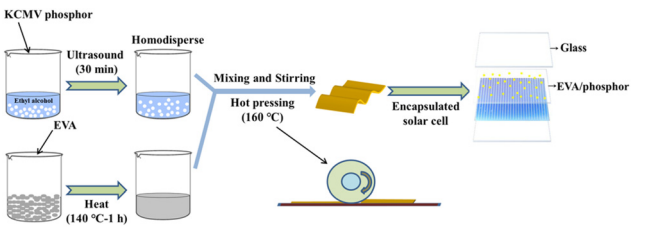

Fig. 1 Preparation process of the EVA/KCMV composite layer and the flow chart of solar cell encapsulation.

NIR spectrometer. The photoelectric conversion external quantum efficiency (EQE) of solar cells was recorded using a solar quantum efficiency test system (Zolix scs10, China) under standard 10 × 10 mm^2 silicon solar cells. The tensile properties of the films were tested using a universal material testing machine (INSTRON 34TM-5, USA).

3. Results and discussion

The XRD data of the KCMV material were refined by the Rietveld method using a structural model in the cubic crystal space group *Ia*3*d*. The refinement converged to an R_{wp} of 5.85%, an R_p of 4.57%, and a goodness of fit (GOF) of 1.02 (shown in Fig. 2a). Fig. 2b depicts the refined crystal structure model. The refined structural parameter information and bond lengths are shown in Tables S1 and S2,† respectively. The presence of a small amount of secondary phase KVO_3 (8.49 wt%, COD: 1527491, space group: *Pbcm*) was observed through the refinement results, while no obvious changes were detected by site occupancy refinement. The refined unit cell parameters can be better described by a = 12.4707(2) Å and volume = 1939.426(1) $Å^3$. In the cubic unit cell, the V1 atom occupies the 24*d* Wyckoff position and bonds with the surrounding four oxygen atoms to form a VO_4 tetrahedral environment (V–O bond length 1.7179 Å). Mg1 atoms occupy the 16*a* Wyckoff position of six-oxygen coordination (bond length 2.129 Å), forming an MgO_6 octahedral environment and co-linking with the VO_4 tetrahedron to form the structural skeleton. Ca1 and K1 atoms are randomly distributed in a ratio of 2 : 1, located at the 24*c* Wyckoff position in holes composed of eight VO_4 and MgO_6 polyhedra, and are coordinated by eight oxygen atoms to form a (Ca, K)O_8 dodecahedron.

Fig. 3a shows the PL and PLE spectra of the KCMV phosphor at room temperature. The KCMV phosphor exhibits a broad absorption band ranging from 250 to 450 nm with the strongest absorption peak at 350 nm. As shown in Fig. 3b, the excitation spectra of the KCMV phosphor can be well fitted into two Gaussian bands at 335 nm and 369 nm, corresponding to the $^1A_1$–$^1T_2$ (Ex_1) and $^1A_1$–$^1T_1$ (Ex_2) transitions in the $(VO_4)^{3-}$ group, respectively.[40–44] Under 350 nm excitation, the KCMV phosphor shows an asymmetric broad emission band centered at 520 nm. This spontaneous emission band originates from the electron charge transfer transitions $^3T_2$–$^1A_1$ (Em_1) and $^3T_1$–$^1A_1$ (Em_2) between O^{2-} and V^{5+} in the $(VO_4)^{3-}$ group.[40,44] These transitions correspond to the Gaussian bands fitted at 510 nm and 565 nm in the emission spectra. Owing to the relatively small energy level difference between the two transitions, an asymmetric wide emission band with a full width at half-maximum (FWHM) of 125 nm is observed in the range of 400–750 nm. The KCMV phosphor has a wide emission range, which has a positive effect on the efficiency of silicon solar cells.

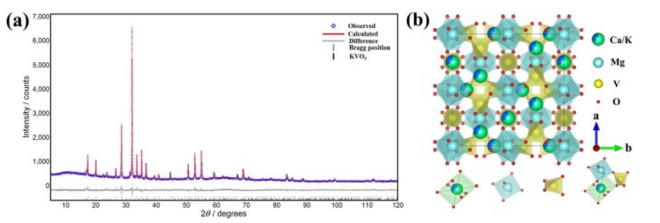

Fig. 2 (a) XRD Rietveld refinement pattern of KCMV (R_{wp} = 5.85%, R_p = 4.57%, and GOF = 1.02); the contents of the main phase KCMV and the minor phase KVO_3 are 91.51 wt% and 8.49 wt%, respectively. (b) Refined crystal structural model of KCMV; the insets show the coordination environments of Ca/K, Mg, and V with oxygen, respectively.

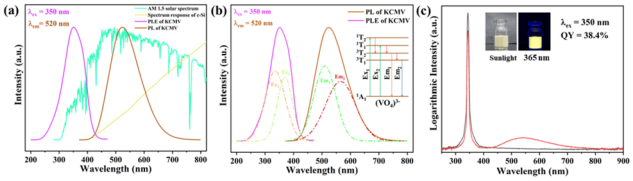

Fig. 3 (a) PL and PLE spectra of the KCMV phosphor. AM 1.5 solar spectrum and the spectral response of c-Si. (b) Gaussian peak fitting spectrogram of the KCMV phosphor. The inset shows the schematic diagram of the luminescence mechanism of the KCMV phosphor. (c) Quantum yield of the KCMV phosphor under a $BaSO_4$ background at 350 nm excitation. The inset shows a digital photograph of the KCMV phosphor in sunlight and ultraviolet light.

In order to evaluate the ability of the KCMV phosphor to modify the solar spectrum, the PLQY data were recorded under the $BaSO_4$ background (as shown in Fig. 3c). The result showed that the KCMV phosphor exhibited a quantum efficiency of 38.4% at an excitation wavelength of 350 nm. It is worth mentioning that the UV absorption and visible broadband emissions of phosphors at higher quantum efficiencies can modify the solar spectrum of silicon solar cells and improve the photoelectric conversion efficiency of solar cells. It is further shown that the phosphor has commendable DS properties of absorbing high-energy UV photons and converting them into visible photons. Combined with the large broadband of the emission spectrum, this shows that the phosphor has the ability to broaden the spectral range that silicon semiconductors can utilize in terms of modifying the solar spectrum of silicon solar cells, helping to enhance the generation of photogenerated electrons and improve the power generation efficiency.

The thermal stability of phosphors will seriously affect the efficiency of solar cells. To study the thermal stability of the KCMV phosphors, temperature-dependent emission spectral tests were conducted in the range of 298–423 K under 350 nm UV excitation, as shown in Fig. 4a. The fluorescence intensities at different temperatures are presented in Fig. 4b. The luminescence intensity decreases obviously with increasing temperature. This temperature rise leads to increased lattice vibration and the growth of thermally activated phonons. Understanding this relationship is crucial for predicting material behavior under varying thermal conditions. Most electrons couple with thermally activated phonons through the

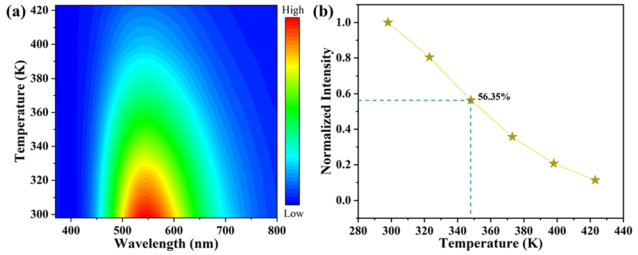

Fig. 4 (a) Temperature-dependent emission spectra of KCMV phosphors (λ_{ex} = 350 nm). (b) Temperature-dependent normalized integrated emission intensity (370–800 nm wavelength range) of KCMV phosphors (λ_{ex} = 350 nm).

ΔE barrier and jump directly from the excited state back to the ground state, resulting in reduced luminescence intensity. It can be seen that the fluorescence intensity decreases to 56.35% of its original value at 348 K, indicating moderate thermal stability. This decrease may be due to energy migration within the $(VO_4)^{3-}$ group at high temperatures, resulting in energy transfer to lattice defects. Higher temperature increases the probability of energy migration and the interaction of excitation energy with lattice defects, leading to greater emission quenching.[45]

In order to better mix the inorganic materials with the EVA colloidal particles, the KCMV phosphor powder was dispersed using ethyl alcohol as the solvent and the particle size of the material was screened through screens of different sizes. The FE-SEM image of the sieved sample is shown in Fig. 5a. Although there are individual aggregates and large particles, the size is uniform and the surface is smooth.

Without considering large agglomerated particles, the statistical distribution of uniformly sized particle sizes in the FE-SEM image was carried out, as shown in Fig. 5b. Normal distribution was fitted to the particle distribution data. At the same time, the average particle size of the KCMV sample after screening is 2–3 μm.

The screened KCMV material was mixed with EVA colloidal particles according to different mass ratios and pressed into an EVA/phosphor film in a vacuum chamber. The transmittance curve of the film is shown in Fig. 6. The transmittance of the pure EVA film can reach 90% in the range of 400–1100 nm. With the introduction of the KCMV material, the transmittance of the film is hindered by powder particles and shows a downward trend, but it is generally maintained above 85%. Compared with the pure EVA film, the high-energy photon absorption of the KCMV material in the UV region causes the transmittance of the EVA/phosphor film to decrease by about 20% in the range of 250–400 nm, which corresponds to the PLE spectrum of the KCMV material (see Fig. 3a). Moreover, the mechanical properties of the film did not change significantly after the addition of the KCMV phosphor, as shown in Fig. S1.† The addition of the KCMV phosphor increases the tensile strain of the film to some extent, especially when the addition concentration is 0.2 wt% and the tensile strain of the film increases by nearly 200%. This may be due to the enhanced interaction between the phosphor and EVA, resulting in a certain improvement in the mechanical properties of the film. This indicates that the phosphor addition did not significantly affect the film's mechanical properties.

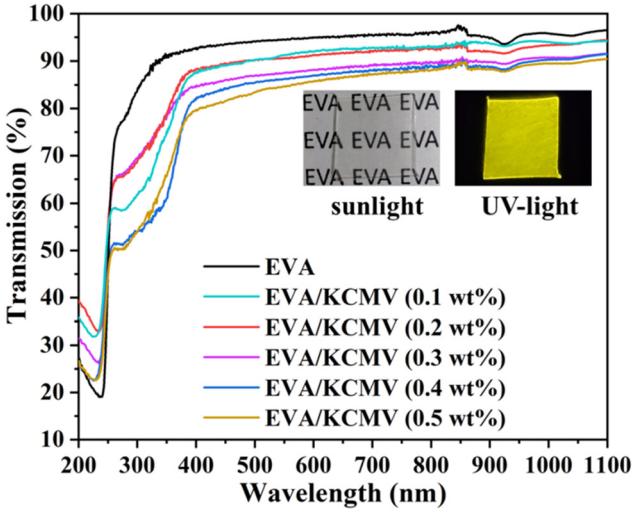

Fig. 6 Transmittance curves of EVA/KCMV films with different amounts of the KCMV phosphor. The inset shows a digital photograph of the EVA/KCMV (0.3 wt%) composite layer in sunlight and ultraviolet light.

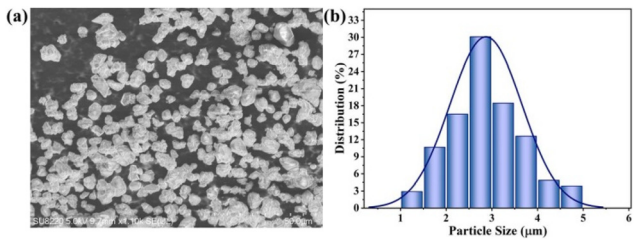

Fig. 5 (a) FE-SEM image of the sieved KCMV phosphor. (b) Particle size distribution histogram of the KCMV phosphor; the purple curve is the Gaussian fitting curve.

It is well known that the valence state of transition metal elements directly affects the physical and chemical properties of materials. To determine the valence state of V ions in the KCMV system and its impact on luminescence, EPR and XPS data were recorded for KCMV, as shown in Fig. 7. V^{5+} is diamagnetic and undetectable by EPR, while significant signal

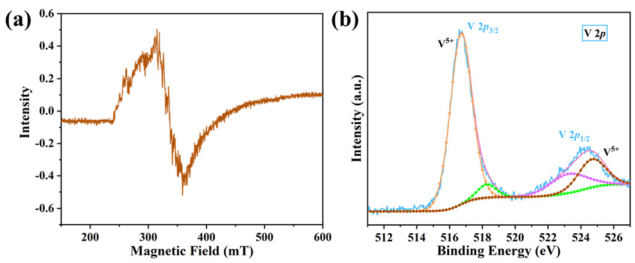

Fig. 7 EPR spectra (a) and XPS spectra (b) of V for KCMV.

peaks in the 250–450 mT range correspond to a *g*-factor of approximately 2. These peaks display several nearly equidistant octets, attributed to the hyperfine coupling of electron spins to the ^{51}V isotope nuclei (nuclear spin $I = 7/2$, natural abundance 100%), indicating the presence of V^{4+} in the KCMV system.[46] Additionally, XPS peaks in the ranges of 517–518 eV/518–519 eV and 522–524 eV/524–526 eV correspond to V^{5+}.[47–49] Combining the EPR and XPS data, it is evident that there is a small amount of V^{4+} in the KCMV phosphor, but most of it is V^{5+}. This ionic valence ratio ensures that V^{4+} has minimal impact on the luminescence performance of the KCMV phosphor.

Fig. 8 depicts the *J–V* characteristic curves and the corresponding *P–V* curves of the bare monocrystalline silicon cell, the monocrystalline silicon solar cell containing an EVA film, and the EVA/KCMV (0.3 wt%) film containing a monocrystalline silicon solar cell in an AM 1.5 simulated solar spectrum environment. The *J–V* characteristic parameters of other solar cells containing EVA films with different KCMV concentrations are listed in Table 1. From the bare monocrystalline silicon solar cell data, it can be clearly found that the short-circuit current density (J_{sc}) and the open-circuit voltage (V_{oc}) of the cell are 33.20 mA cm^{-2} and 0.6147 V respectively, and the power conversion efficiency (PCE) is 15.11%. The J_{sc} and V_{oc} values of the solar cell containing the EVA film increased to 33.84 mA cm^{-2} and 0.6370 V, respectively. It is worth mentioning that although the pure EVA film has an impact on the transmission of the simulated sunlight, the tight packaging of the solar cells by EVA can accurately and effectively reduce the refraction and scattering of the simulated sunlight in the atmosphere, thus improving the performance of the solar cell (the PCE increased to 15.33%). Through analysis of the *J–V* characteristic data of EVA/KCMV solar cells with different phosphor contents, it can be found that the introduction of a DS phosphor will affect the photoelectric conversion performance of solar cells to a certain extent. When the content of KCMV is 0.3 wt%, the performance parameters of the solar cell become optimal, with the J_{sc} and V_{oc} values reaching 34.16 mA cm^{-2} and 0.6451 V respectively. Compared with the J_{sc} and V_{oc} values of the pure EVA solar cell, they are increased by 0.95% and 1.27% respectively. At the same time, the PCE of solar cells reaches the maximum, which is increased by 4.17% compared to the pure EVA solar cell, reaching 15.97%. The existence of fluorescent materials indirectly improves the utilization range of silicon solar cells for simulated sunlight. KCMV can effectively convert the UV region of simulated sunlight into visible light that silicon cells can directly absorb and utilize. This undoubtedly increases the output of photogenerated electron pairs in silicon cells per unit time, thereby increasing the potential difference and current density at both ends of the cell. Of course, the improvement of solar cell performance will not continue to show a linear relationship with the content of phosphor. The accumulation of a large amount of powder in the EVA will also hinder the ability of the silicon cells to capture sunlight.

The reflectance test of solar cells under different configurations is only to further confirm that the improvement in solar cell performance comes from the KCMV phosphor. Fig. 9 shows the reflectance curves and absorption spectra of the

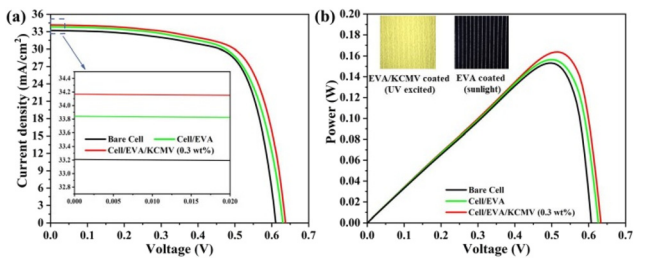

Fig. 8 (a) *J–V* characteristics curves and (b) *P–V* curves of monocrystalline silicon solar cells with different configuration conditions in an AM 1.5 simulated solar spectrum environment (bare cell, pure EVA-encapsulated solar cell and EVA/KCMV (0.3 wt%)-encapsulated solar cell). The inset shows a digital photograph of the solar cell coated with an EVA/KCMV (0.3 wt%) composite layer irradiated with sunlight and ultraviolet (UV) light.

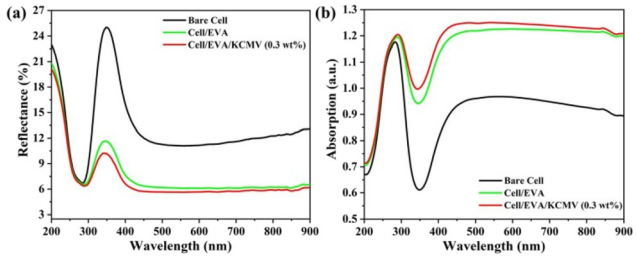

Fig. 9 Reflectivity (a) and absorptivity (b) curves of different monocrystalline silicon solar cells (bare cell, pure EVA-encapsulated solar cell and EVA/KCMV (0.3 wt%)-encapsulated solar cell).

Table 1 *J–V* characteristics of solar cells with different KCMV phosphor concentrations

Type of solar cell	J_{sc} (mA cm^{-2})	V_{oc} (V)	P_{max} (W)	FF (%)	PCE (%)	Relative increase of PCE (%)
Bare cell	33.20	0.6147	0.2342	74.06	15.11	—
Cell/EVA	33.84	0.6370	0.2376	71.12	15.33	1.46
Cell/EVA/KCMV (0.1 wt%)	34.03	0.6408	0.2410	71.30	15.55	2.91
Cell/EVA/KCMV (0.2 wt%)	34.07	0.6417	0.2451	72.33	15.81	4.63
Cell/EVA/KCMV (0.3 wt%)	**34.16**	**0.6451**	**0.2475**	**72.46**	**15.97**	**5.69**
Cell/EVA/KCMV (0.4 wt%)	33.81	0.6406	0.2423	72.18	15.63	3.44
Cell/EVA/KCMV (0.5 wt%)	33.35	0.6397	0.2367	71.61	15.27	1.06

bare silicon cell, solar cells encapsulated with the pure EVA film and the EVA/KCMV (0.3 wt%) film. Compared with the bare silicon cell, solar cells encapsulated with the EVA film have lower reflectivity in the range of 200–900 nm. The reasons for this change can be explained based on the following two aspects. The first is that the KCMV material with the DS luminescence effect absorbs high-energy UV photons and emits lower-energy visible light in the 300–400 nm range, resulting in a final 16% reduction in the reflectivity of the solar cell. On the other hand, the scattering of light by the KCMV material particles causes the EVA/KCMV-encapsulated solar cell to enhance the absorption of incident light sources in the range of 400–900 nm (a relative increase of 32%, as shown in Fig. 9b). It is worth mentioning that this ability to capture incident light is very important in the practical application of solar cells.[50,51] Due to the special adhesiveness of EVA materials, the pure EVA-encapsulated solar cell shows a reflectivity that is 13% lower than that of the bare silicon cell after isolating atmospheric scattering. At the same time, the lower average refractive index of EVA (n = 1.48–1.49) reduces the Fresnel reflection loss when absorbing incident light.[52,53] It is worth noting that in order to prevent the spectral conversion film from offsetting the potential improvement in the solar cell performance of DC/DS fluorescent materials, the film must have high visible light transmittance while also having strong UV absorption and low overall reflectivity.

In order to more intuitively demonstrate the improvement in photoelectric conversion efficiency of solar cells, EQE characterization of solar cells in different configurations was performed under AM 1.5 simulated light sources (shown in Fig. 10). Among them, the bare silicon cell showed about 90% of the photoelectric conversion efficiency in the visible optical region, and the introduction of the EVA film reduced the reflection of simulated solar light and reduced the atmospheric scattering, improving the photoelectric conversion efficiency of solar cells. Of course, the EVA/KCMV film-encapsulated solar cell exhibits better conversion efficiency in the full wavelength band (300–1100 nm) and shows a maximum conversion efficiency of more than 19% (relative to the bare silicon cell) in the UV region. This clearly shows that the improvement in photoelectric conversion efficiency is mainly due to the KCMV phosphor absorbing UV light and releasing

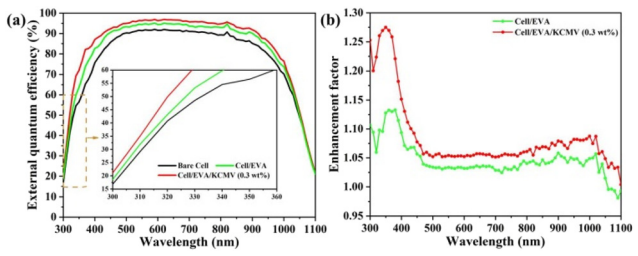

Fig. 10 (a) EQE curves of different monocrystalline silicon solar cells in an AM 1.5 environment. (b) Enhancement factor of EQE for solar cells (bare cell, pure EVA-encapsulated solar cell and EVA/KCMV (0.3 wt%)-encapsulated solar cell).

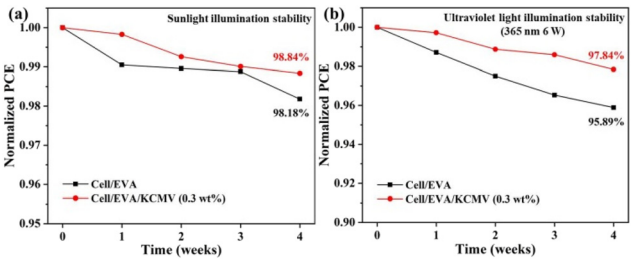

Fig. 11 Device efficiency stability of solar cells containing EVA and EVA/KCMV (0.3 wt%) under sunlight (a) and ultraviolet light(b).

visible light. The converted photons are absorbed and consumed on the surface of the monocrystalline silicon, and the generated photogenerated electron–hole pairs are rapidly separated under the action of an external electric field, forming a greater potential difference and current density at the positive and negative ends of the solar cell. In other words, the presence of the KCMV material increases the number of photons of visible light absorbed by monocrystalline silicon and broadens the actual usable solar spectrum range of monocrystalline silicon. At the same time, combined with the absorption curve in Fig. 9b, the improvement in conversion efficiency in the visible light region is due to the impact of the EVA and the KCMV material on the convergence and capture of incident light.

To explore the effect of KCMV fluorescent powder on the stability of silicon solar cell devices, solar cells coated with fluorescent powder and pure EVA were tested for efficiency changes under sunlight and UV light for 4 weeks, as shown in Fig. 11. The lowest temperature during the four weeks was 0 °C; the highest was 21 °C with an average temperature difference of 9.5 °C between day and night. After 4 weeks, the efficiency of solar cells containing KCMV (0.3 wt%) under sunlight was 98.84% of the original, while the efficiency of solar cells containing pure EVA was 98.18%. This change was not significant under sunlight, which is attributed to the stability of silicon itself and the weaker UV radiation under sunlight. However, the change was particularly pronounced under UV light, with the efficiency of solar cells containing fluorescent powder being 97.84% of the original, compared to 95.89% for those containing pure EVA. The specific photovoltaic parameter changes are shown in Fig. S2.† The efficiency of solar cells containing pure EVA decreased significantly compared to those containing fluorescent powder, mainly because the down-shift effect of KCMV phosphors enhanced the utilization of UV light by the solar cells, reducing the impact on the device. Thus, the addition of KCMV fluorescent powder can not only improve the conversion efficiency of solar cells, but also enhance their stability, prolonging the device's lifespan.

4. Conclusions

In this work, we developed a phosphor that is easy to prepare and exhibits a DS effect, which was mixed with the EVA

material as a spectrum conversion material and applied to the surface of monocrystalline silicon solar cells. This approach is applicable not only to the KCMV phosphor, but also to other inorganic luminescent materials. Our findings demonstrate that the KCMV phosphor with a DS effect can effectively broaden the wavelength range of the solar spectrum absorbed by silicon solar cells. The experimental results show that solar cells containing an EVA/KCMV (0.3 wt%) film achieved the highest photoelectric conversion efficiency, with a 5.69% increase compared to bare silicon cells (from 15.11% to 15.97%), and the current density increased by 2.89% (from 33.20 to 34.16 mA cm^{-2}). This work employs inorganic solid materials as the core of the spectrum converter, offering high luminous efficiency, strong spectral adaptability, environmental friendliness, and high stability. These attributes suggest potential applications in other types of photovoltaic devices in the future.

Data availability

All data supporting this article have been included in the manuscript or included as part of the ESI.†

Conflicts of interest

There are no conflicts to declare.

Acknowledgements

This paper was supported by the National Natural Science Foundation of China (51972203 and 22271180) and Fundamental Research Funds for the Central Universities (GK202304054).

References

1 M. Usman and D. Balsalobre-Lorente, *Energy Policy*, 2022, **162**, 112780.
2 P. T. Ogunboyo and O. Ogunlade, *Appl. Photovoltaic Technol.*, 2024, **1**, 323.
3 A. Koerdt, J. Samojluk and B. A. A. Stepec, in *Petroleum Microbiology*, CRC Press, 2024, pp. 191–232.
4 P. Yang, in *Renewable Energy: Challenges and Solutions*, Springer, 2024, pp. 1–36.
5 C. M. S. Kumar, S. Singh, M. K. Gupta, Y. M. Nimdeo, R. Raushan, A. V. Deorankar, T. M. A. Kumar, P. K. Rout, C. S. Chanotiya, V. D. Pakhale and A. D. Nannaware, *Sustainable Energy Technol.*, 2023, **55**, 102905.
6 N. R. E. Laboratory, Best Research-Cell Efficiency Chart.
7 A. M. Adeyinka, O. V. Mbelu, Y. B. Adediji and D. I. Yahya, *Int. J. Energy Power Eng.*, 2023, **17**, 1–10.
8 A. Khan, M. Khan, N. Ahmed, Z. A. Khan and M. Z. Zahir, *Nanomaterials for Energy Applications*, 2024, pp. 5–31.
9 N. S. Satpute, C. M. Mehare, A. Tiwari, H. C. Swart and S. J. Dhoble, *ACS Appl. Electron. Mater.*, 2022, **4**, 3354–3391.
10 D. Yu, T. Yu, H. Lin, S. Zhuang and D. Zhang, *Adv. Opt. Mater.*, 2022, **10**, 2200014.
11 C. Chen, X. Xie, M. Yang, H. Zhang, I. Seok, Z. Guo, Q. Jiang, G. Wangila and Q. Liu, *ES Energy Environ.*, 2021, 3–18.
12 A. Ghazy, M. Safdar, M. Lastusaari, H. Savin and M. Karppinen, *Sol. Energy Mater. Sol. Cells*, 2021, **230**, 111234.
13 Z. Chen, H. Jia, K. Sharafudeen, W. Dai, Y. Liu, G. Dong and J. Qiu, *J. Alloys Compd.*, 2016, **663**, 204–210.
14 B. Qu, Y. Jiao, S. He, Y. Zhu, P. Liu, J. Sun, J. Lu and X. Zhang, *J. Alloys Compd.*, 2016, **658**, 848–853.
15 J. Wang, T. Ming, Z. Jin, J. Wang, L.-D. Sun and C.-H. Yan, *Nat. Commun.*, 2014, **5**, 5669.
16 G. E. Arnaoutakis, J. Marques-Hueso, A. Ivaturi, K. W. Krämer, S. Fischer, J. C. Goldschmidt and B. S. Richards, *Opt. Express*, 2014, **22**, A452.
17 T. Trupke, M. Green and P. Würfel, *J. Appl. Phys.*, 2002, **92**, 1668–1674.
18 B. S. Richards, *Sol. Energy Mater. Sol. Cells*, 2006, **90**, 1189–1207.
19 A. Verma and S. K. Sharma, *ECS J. Solid State Sci. Technol.*, 2023, **12**, 116004.
20 A. R. Kadam and S. J. Dhoble, *J. Alloys Compd.*, 2021, **884**, 161138.
21 G. R. S. Mattos, C. D. S. Bordon, L. A. Gómez-Malagón, R. M. Gunji and L. R. P. Kassab, *J. Lumin.*, 2021, **238**, 118271.
22 M. Derouiche, R. Salhi and S. Baklouti, *J. Radiat. Res. Appl. Sci.*, 2023, **16**, 100497.
23 P. S. David, P. Panigrahi, S. Raman and G. S. Nagarajan, *Mater. Sci. Semicond. Process.*, 2021, **122**, 105486.
24 N. B. Aranda, R. F. Muniz, M. L. Baesso, A. C. Bento, H. M. S. Deroide, A. N. Medina, L. A. O. Nunes, J. R. Silva, S. M. Lima, L. H. C. Andrade and J. H. Rohling, *Opt. Mater.*, 2023, **142**, 114060.
25 R. Reddappa, K. Suresh and C. K. Jayasankar, *Opt. Mater.*, 2021, **122**, 111700.
26 D. O. Kumi, S. Khan, S.-H. Cho and M. O. Ntwaeaborwa, *Physica B*, 2020, **576**, 411711.
27 H. Yao and Q. Tang, *Sol. Energy*, 2020, **211**, 446–452.
28 R. Elleuch, R. Salhi, S. I. Al-Quraishi, J. L. Deschanvres and R. Maâlej, *Phys. Lett. A*, 2014, **378**, 1733–1738.
29 F. Aouaini, A. Maaoui, N. B. H. Mohamed, M. M. Alanazi and L. A. El Maati, *J. Alloys Compd.*, 2022, **894**, 162506.
30 S. K. Karunakaran, C. Lou, G. M. Arumugam, C. Huihui and D. Pribat, *Sol. Energy*, 2019, **188**, 45–50.
31 J. Liu, K. Wang, W. Zheng, W. Huang, C. H. Li and X. Z. You, *Prog. Photovoltaics*, 2012, **21**, 668–675.
32 K. Yuwawech, J. Wootthikanokkhan and S. Tanpichai, *Polym. Test.*, 2015, **48**, 12–22.
33 J. Zhou, F. Huang, J. Xu, H. Chen and Y. Wang, *J. Mater. Chem. C*, 2015, **3**, 3023–3028.

34 T. Nakajima, M. Isobe, Y. Uzawa and T. Tsuchiya, *J. Mater. Chem. C*, 2015, **3**, 10748–10754.
35 T. Nakajima, M. Isobe, T. Tsuchiya, Y. Ueda and T. Kumagai, *Nat. Mater.*, 2008, **7**, 735–740.
36 H. Guo, B. Devakumar, R. Vijayakumar, P. Du and X. Huang, *RSC Adv.*, 2018, **8**, 33403–33413.
37 X. Huang and H. Guo, *RSC Adv.*, 2018, **8**, 17132–17138.
38 *B. A. TOPAS, V5.0: General Profile and Structure Analysis Software for Powder Diffraction Data*, Karlsruhe, Germany.
39 J. C. de Mello, H. F. Wittmann and R. H. Friend, *Adv. Mater.*, 2004, **9**, 230–232.
40 X. Huang and H. Guo, *Dyes Pigm.*, 2018, **154**, 82–86.
41 R. Cao, X. Wang, Y. Jiao, X. Ouyang, S. Guo, P. Liu, H. Ao and C. Cao, *J. Lumin.*, 2019, **212**, 23–28.
42 P. Du, L. Zhou, L. Luo and J. S. Yu, *New J. Chem.*, 2019, **43**, 6688–6695.
43 L. K. Bharat, S.-K. Jeon, K. G. Krishna and J. S. Yu, *Sci. Rep.*, 2017, **7**, 42348.
44 E. Pavitra, G. S. R. Raju, J. Y. Park, L. Wang, B. K. Moon and J. S. Yu, *Sci. Rep.*, 2015, **5**, 10296.
45 A. Setlur, H. Comanzo, A. Srivastava and W. Beers, *J. Electrochem. Soc.*, 2005, **152**, H205.
46 M. Kindle, S. Kmiec, I. d'Anciães Almeida Silva, H. Eckert, S. W. Martin, M.-K. Song and J. S. McCloy, *J. Non-Cryst. Solids*, 2019, **521**, 119551.
47 N. Nag and F. Massoth, *J. Catal.*, 1990, **124**, 127–132.
48 Y. Schuhl, H. Baussart, R. Delobel, M. Le Bras, J.-M. Leroy, L. Gengembre and J. Grimblot, *J. Chem. Soc., Faraday Trans.*, 1983, **79**, 2055–2069.
49 F. J. Berry, M. E. Brett, R. A. Marbrow and W. R. Patterson, *J. Chem. Soc., Dalton Trans.*, 1984, 985–987.
50 S. Hore, C. Vetter, R. Kern, H. Smit and A. Hinsch, *Sol. Energy Mater. Sol. Cells*, 2006, **90**, 1176–1188.
51 X. Pi, Q. Li, D. Li and D. Yang, *Sol. Energy Mater. Sol. Cells*, 2011, **95**, 2941–2945.
52 M. C. Wei, S. J. Chang, C. Y. Tsia, C. H. Liu and S. C. Chen, *Sol. Energy*, 2006, **80**, 215–219.
53 R. H. French, J. M. Rodríguez-Parada, M. K. Yang, R. A. Derryberry and N. T. Pfeiffenberger, *Sol. Energy Mater. Sol. Cells*, 2011, **95**, 2077–2086.